

PAPER • OPEN ACCESS

Controllable non-ideal plasmas from photoionized compressed gases

To cite this article: Gautham Dharuman *et al* 2018 *New J. Phys.* **20** 103010

View the [article online](#) for updates and enhancements.



IOP | ebooks™

Bringing you innovative digital publishing with leading voices to create your essential collection of books in STEM research.

Start exploring the collection - download the first chapter of every title for free.



OPEN ACCESS

RECEIVED
30 April 2018REVISED
8 September 2018ACCEPTED FOR PUBLICATION
24 September 2018PUBLISHED
10 October 2018

Original content from this
work may be used under
the terms of the [Creative
Commons Attribution 3.0
licence](#).

Any further distribution of
this work must maintain
attribution to the
author(s) and the title of
the work, journal citation
and DOI.



PAPER

Controllable non-ideal plasmas from photoionized compressed gases

Gautham Dharuman^{1,3}, Liam G Stanton² and Michael S Murillo¹¹ Department of Computational Mathematics, Science and Engineering, Michigan State University, East Lansing, MI 48824, United States of America² Department of Mathematics & Statistics, San José State University, San José, CA 95192, United States of America³ Author to whom any correspondence should be addressed.E-mail: dharuman@msu.edu, liam.stanton@sjsu.edu and murillom@msu.edu**Keywords:** strongly coupled plasma, photoionized gas, molecular dynamics, continuum lowering, equation of state, plasma transport

Abstract

Based on a suite of molecular dynamics simulations, we propose a strategy for producing non-ideal plasmas with controllable properties over a wide range of densities between those of ultracold neutral plasmas and those of solid-density plasmas. We simulated the formation of non-equilibrium plasmas from photoionized, cool gases that are spatially precorrelated through neutral–neutral interactions that are important at moderate-to-high pressures. A wide range of physical properties, including Coulomb collisional rates, partial pressures, screening strengths, continuum lowering, interspecies Coulomb coupling, electron degeneracy and ionization states, were characterized across more than an order of magnitude variation in the initial gas pressure. A wide range of plasma properties are also found to vary when the initial pressure of a precorrelated gas is varied. Thus, we propose that non-ideal plasmas with tunable properties can be generated by photo-ionizing a dense, precorrelated gas. We find that the optimal initial density range for the gas is near a Kirkwood/Widom–Fisher line in the neutral-gas phase diagram. This strategy for generating non-ideal plasmas suggests experiments that have significant advantages over both ultracold and solid-density plasma experiments because the collisional, collective and recombination timescales can be tuned across many orders of magnitude, potentially allowing for a wider range of diagnostics. Moreover, the added costs of cooling ultracold plasmas and diagnosing dense matter with x-rays are eliminated.

1. Introduction

The physics of non-ideal plasmas is important in a wide range of applications, including exploding wires [1–3], late-stage stellar evolution [4–8], interiors of giant planets [9], x-ray free electron laser (XFEL) experiments [10–13], inertial-confinement fusion (ICF) experiments [14], dusty plasmas [15–20], condensed matter [21–23], non-neutral plasmas [24–27], and ultracold neutral plasmas (UCNPs) [28–37]. Each of these applications explores specific, narrow ranges of densities and temperatures and utilizes highly variable diagnostics. For example, dusty plasmas tend to form very strongly coupled monolayers that can be diagnosed at the individual particle level; however, it is more difficult to create three-dimensional, moderately coupled plasmas [15]. Similarly, solid-density plasmas are generated at very high pressures, which yield highly transient and unstable states that are difficult to probe without large-scale facilities [13, 38–40]. In contrast, UCNPs require extremely low temperatures and are difficult to produce in the strongly coupled regime [41, 42]. Moreover, dusty plasmas and UCNPs are dominated by classical physics, whereas dense plasmas tend to be electronically quantum; one can transition smoothly between classical and quantum physics by isochorically heating a solid, but such experiments tend to be very expensive because the lasers involved in producing and diagnosing a plasma often require specialized XFEL facilities.

Given these considerations, it would be useful to have an alternate table-top method that allows for wide and continuous variations in density with independent control over the temperature and ionization state, including

two-temperature variations (i.e., separate electron and ion temperatures). The desired method would allow for systematic control of plasma properties, including transport and relaxation, ionization-potential depression (IPD), the non-ideal multi-temperature equation of state (EOS), and screening involving strongly coupled electrons. Transport properties [43, 44] and relaxation processes [45–48] are important to validate and model dense plasma experiments. The advent of XFEL [49–51] has renewed interest in IPD (*a.k.a.* ‘continuum lowering’), and dense plasma experiments have been used to validate different IPD models [52–55]. An accurate EOS is essential for examining plasma evolution on the hydrodynamic scale, such as the evolution of fluid instabilities in ICF experiments [56, 57] or UCNP expansion into a vacuum [29]. Strongly coupled electrons, which are difficult to create at high densities because of degeneracy, have been of theoretical and experimental interest for several decades [21, 22], including, more recently, for their role in the conductance of liquid-helium surfaces [23]. Finally, such an approach could also serve as a platform for measuring coupled electron–ion modes, which have been of recent interest in dense two-temperature plasmas [58]. In fact, isolated experiments at these intermediate densities have been performed successfully [59–61]; however, controllability and tunability of plasma properties were not the focus of those experiments. Here, we present a unified approach for studying all of these properties over a wide range of coupling strengths, tuned with the initial pressure of the neutral gas.

Based on a large suite of molecular dynamics (MD) simulations, we propose an experimental procedure for creating three-dimensional non-ideal plasmas with controllable properties at densities between those of UCNP and those of dense plasmas (defined here as plasmas created through shock or radiation heating of a solid or liquid). Our new paradigm builds upon previously successful examples of similar methods applied to UCNP that employ a cold, photoionized gas at very low density [33]. UCNP experiments, however, are plagued by the process of disorder-induced heating (DIH) [31, 41], which prevents strong coupling despite plasma creation from ultracold gases (the ionic temperature immediately after ionization can be $\sim 10^{-6}$ K). DIH occurs as a consequence of creating a plasma in a non-equilibrium state [42]; the excess potential energy in the system is rapidly converted into kinetic energy. Mitigating DIH requires a precorrelated state (prior to ionization) [41], and strong coupling between ions has been shown to be theoretically possible in degenerate Fermi gases [41], Rydberg-blockaded gases [62] and optical lattices [63], all of which require very low temperatures. We employ a novel paradigm for precorrelation: compressing gases to high pressures at room temperature, thereby reducing the burden of trapping and cooling to extremely low temperatures. As with other plasmas produced through photoionization, this procedure allows the electron temperature to be tuned independently of the ion temperature, thereby permitting two-temperature studies in the non-ideal regime. Moreover, by operating at densities lower than solid, physical time scales of interest (e.g., collisional and collective) are effectively stretched (relative to dense plasma experiments [10–12]), and a wider range of diagnostics potentially becomes available.

The manuscript is organized as follows. In section 2, we propose an approach to mitigate DIH through pressure-induced precorrelation. Next, in section 3, we give an overview of the computational methods used to predict the behavior of materials under these conditions. Our results are presented in section 4 in terms of IPD, transport phenomena and EOS. Finally, conclusions are given in section 5.

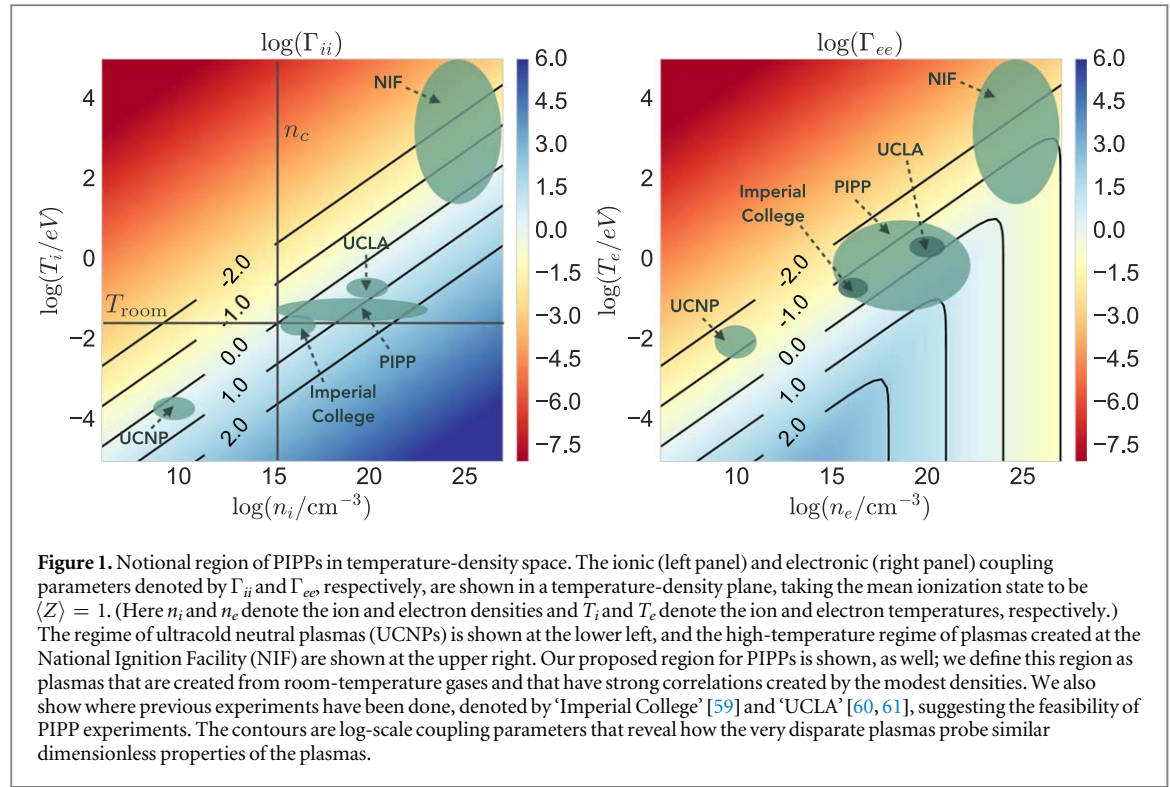
2. Mitigation of DIH: pressure-induced precorrelation

Forming plasmas at low densities has numerous advantages, including the ability to control the ionization state, allowing for table-top visible lasers as probes and the relatively slow time scales associated with collisions and collective phenomena. However, DIH limits the Coulomb coupling parameter to an order of unity unless some mechanism for precorrelation is employed [64]. For this reason, cooling a gas to temperatures well below the DIH temperature has limited advantages. Conversely, in the extreme limit of employing a solid or liquid as a target, the ions are highly precorrelated [65, 66]; in fact, these systems can be viewed as ‘overcorrelated’ [67]. Such dense targets can be isochorically heated to various temperatures to achieve a range of plasma conditions. However, because of the high densities and pressures, these plasmas require large facilities for their creation and diagnosis.

To motivate our strategy, we review the process of DIH that occurs following photoionization of a neutral gas. The initial temperature T_0 and the final temperature T_f are related to the spatial correlations in the initial and final states by [41]

$$T_f = T_0 + \frac{1}{3} \int \frac{d\mathbf{k}}{(2\pi)^3} \frac{v(k)}{\epsilon(k)} [S_0(\mathbf{k}, T_0) - S_f(\mathbf{k}, T_f)], \quad (1)$$

where $S_0(\mathbf{k}, T_0)$ and $S_f(\mathbf{k}, T_f)$ are the initial and final ion–ion structure factors, respectively, $v(k) = 4\pi e^2/k^2$ is the Coulomb potential in Fourier space, and $\epsilon(k)$ is the dielectric response function. Because of the very large electron–ion mass ratio, the ion–ion collisions associated with the DIH process are much faster than electron–ion collisional processes, and this allows us to neglect any changes in the electrons during DIH. As a result, $\epsilon(k)$ is



approximately constant during that short time interval (about one ionic plasma period [42]). Thus, to achieve large ion–ion coupling after DIH, an initial state with correlations similar to those of the desired plasma is needed.

Because of the issues mentioned above with ultracold and dense plasma experiments, we have examined DIH for modest temperatures at densities that lie *between* those of UCNPs and dense plasmas. To mitigate DIH in this intermediate density range, we propose precorrelating the neutral gas through strong neutral–neutral interactions. This is most easily accomplished by increasing the gas pressure to achieve various levels of precorrelation before ionization; photoionization is then used to form a two-temperature plasma. For conciseness, we will refer to a plasma formed through this procedure as a ‘pressure-induced precorrelated plasma’ (PIPP), and the basic idea is illustrated in figure 1. The ionic and electronic Coulomb couplings are shown in the left and right panels of the figure, respectively, where the mean ionization state has been taken to be $\langle Z \rangle = 1$. At very low density, but higher than that typical of UCNPs, neutral–neutral interactions are very weak. In this low-density regime, DIH leads to a final coupling parameter of order unity [41]; using this fact, we can solve for the DIH temperature (denoted by T_{DIH}) as a function of density:

$$T_{\text{DIH}} \approx \langle Z \rangle^2 e^2 \left(\frac{4\pi n_i}{3} \right)^{1/3}, \quad (2)$$

where n_i is the ion density and e is the fundamental charge. T_{DIH} becomes of order room temperature (denoted by T_{room}) at a density of approximately $n_c = 1.4 \times 10^{15} \text{ cm}^{-3}$ for $\langle Z \rangle = 1$. For densities in this range and above, there is little advantage to cooling the gas before ionization; this is indicated by a horizontal line at T_{room} , and the critical density n_c is shown as a vertical line in the figure. These lines set the lower density and temperature limits of the PIPP regime in figure 1. The contours in the figure are the logarithm of the Coulomb coupling; if there were no correlations, the plasma could evolve through DIH to the contour labeled ‘0.0’, which sets the upper bound for PIPPs, as that state is already achievable with lower-density plasmas. Thus, in the PIPP region, a plasma can be formed from an uncooled gas, and any precorrelation from the modest density is expected to lead to a coupling parameter exceeding unity. The feasibility of producing plasmas in this manner should be addressed: a literature search revealed two experiments, labeled ‘UCLA’ [60, 61] and ‘Imperial College’ [59] in the figure, that fall near the PIPP regime. We also show a portion of the regime accessible by experiments at the National Ignition Facility (NIF); we note that PIPPs would, in principle, provide a platform for exploring physics relevant to NIF on a smaller scale, as can be seen by the constant coupling contours shared by both the PIPP regime and the NIF regime.

There are two main factors that dictated our choice of the candidate gas: (1) we preferred a gas that was used in one of the recent experiments that have conditions similar to PIPPs; this would favor the feasibility of the PIPP paradigm, (2) the size of the atoms constituting the gas must be such that the average interatomic distance in the

neutral gas state is similar to the average separation between the ions in the plasma state; this is an important requirement for DIH mitigation that follows from the discussion on DIH, as described above. The ‘UCLA’ experiments are some of the recent experiments that have conditions similar to PIPPs; these experiments employed helium, argon and xenon (Xe). Among the choices, Xe offers the largest interatomic separation in its neutral state that is similar to the average separation between Xe ions in the plasma state. For the above reasons, we have chosen to study neutral Xe gas in this work. We consider Xe at a temperature of 300 K, which is above its critical point [68], thereby avoiding liquid droplet formation. In the next section, we will discuss the computational models used for our studies of PIPPs generally, and dense Xe in particular.

3. Computational methods

Our primary approach is to employ a variety of MD models using effective pair potentials to simulate the process of creating PIPPs over a wide range of densities. Because PIPPs are created out of equilibrium and tend toward a two-temperature state, methods such as path integral Monte Carlo (PIMC) [69] and Kohn–Sham–Mermin density functional theory (DFT) [70] cannot be applied. PIMC is formulated around an equilibrium thermodynamic density matrix, and DFT formulations assume an equilibrium Fermi–Dirac distribution for the electrons; neither approach applies to a wide range of plasma experiments. Moreover, as PIPPs can span the classical to quantum regimes, PIMC and DFT would be extremely inefficient computationally. In this section, we describe computational methods appropriate to PIPPs.

We employ non-equilibrium MD using several interparticle potentials. The different potentials, described in detail below, are needed to model the neutral gas and the plasma state, including potentials needed to explore strong electron–ion coupling. We use a standard MD approach that employs a velocity–Verlet integrator, a Berendsen thermostat and periodic boundary conditions; typically, for each simulation, 10^4 or more particles were used. An equilibration phase was used for equilibrium simulations of the initial gas and for examinations of equation-of-state issues; otherwise, the simulations were non-equilibrium (e.g., entering the plasma state from the neutral state).

In section 3.1, we discuss the range of potentials needed to explore PIPP behavior using this MD approach. Three classes of potentials are needed to describe PIPPs. To examine precorrelation prior to ionization, we require an accurate neutral–neutral potential. Following ionization, we begin with the equilibrated initial state formed by the neutrals and evolve according to an effective ion–ion potential. For studies that involve details of the electronic state of the PIPP, we further require potentials that can be used to evolve the electrons as an independent species. Because the plasma potentials rely on knowledge of the atomic states, we discuss our generalized Saha model in section 3.2.

3.1. Interparticle interactions

Precorrelation in the neutral gas can be modeled using MD with an appropriate neutral–neutral potential. While a wide range of potentials exist for this case, such as the commonly used Lennard–Jones potential, we employed a potential chosen specifically for Xe. The neutral Xe–Xe interactions are known to be well described over a range of pressures by the exponential-6 (E6) potential [71–73]

$$u_{\alpha\gamma}^{\text{E6}}(r) = \frac{6\varepsilon}{\eta - 6} \left[e^{\eta(1-r/\sigma)} - \frac{\eta}{6} \left(\frac{\sigma}{r} \right)^6 \right], \quad (3)$$

where r is the distance between two atoms, $\varepsilon/k_B = 243.1$ K, $\eta = 13$, and $\sigma = 4.37$ Å [73]. After equilibration, the gas is photoionized, and the interactions become dominated by Coulomb forces.

We do not directly model the ionization process, but rather assume that each neutral is instantly converted to an ion and that the formation of electronic screening clouds is rapid. The time scales involved are those of laser ionization, electron scattering, and ion equilibration. As the ionization is occurring, the electron subsystem equilibrates on a time scale of inverse electron plasma frequency, forming screening clouds around the ions. Subsequently, the ions respond on a time scale of the inverse ion plasma frequency, which is ~ 100 – 1000 times larger than the electron equilibration time scale. This ordering of the time scales is a valid assumption; however, for further validation, MD coupled with atomic kinetics is required. Further, we have assumed that 100% of the neutrals are ionized. When the ionization is below 100%, neutrals will start playing a role; however, their impact on DIH mitigation is unclear. It is possible that the advantages of precorrelation are minimized by the presence of the neutrals. On the contrary, since the neutrals are much less energetic than the ions, it is also possible that the neutral subsystem serves as a cooling bath for the ions, thereby mitigating DIH even further. In order to examine these different possibilities, it is required to perform MD with explicit ion–neutral and neutral–neutral interactions in addition to ion–ion interactions for different ionization fractions. Such detailed simulations to further examine our assumptions would be the focus of future work. Within the assumptions we have made, we

use the (precorrelated) final conditions from the neutral gas simulation as the initial conditions of the plasma simulation and evolve according to a plasma potential relevant for ion–ion interactions at the appropriate ionization level (see the following subsection for a more detailed discussion of our ionization model).

An accurate MD model for ion–ion interactions in this moderately dense regime is the Yukawa potential [41], which is given in Gaussian-cgs units by

$$u_{\alpha\gamma}^Y(r) = \frac{Z_\alpha Z_\gamma e^2}{r} e^{-r/\lambda_e}. \quad (4)$$

Here, Z_α is the charge number of the α th ion and λ_e is the degeneracy-corrected electron-screening length [74] (also referred to as Thomas–Fermi screening length) approximated by

$$\lambda_e^2 \approx \frac{\sqrt{T_e^2 + \left(\frac{2}{3}E_F\right)^2}}{(4\pi e^2 n_e)}, \quad (5)$$

where T_e is the electron temperature (in energy units), and $E_F = \hbar^2(3\pi^2 n_e)^{2/3}/2m_e$ is the electron Fermi energy for electron density n_e . We choose $Z_\alpha = \langle Z \rangle$ for all ions, where the mean ionization $\langle Z \rangle$ is calculated using a non-ideal Saha equation [75–77]; see section 3.2 for details. The Yukawa potential has found wide use in dusty plasmas [78] and UCNPs [79] and has been analyzed in detail recently for dense plasmas [80]. Depending on the PIPP conditions, more development of the ion–ion potential may be called for; for example, as the electron–electron coupling is varied, PIPPs can explore a wider variety of potentials beyond the basic Yukawa potential. The Yukawa potential also neglects ionic core–core interactions beyond the Coulomb interaction; such interactions will be the subject of future work. For these initial studies, we employ the basic Yukawa form (4).

Despite the utility of the E6 and Yukawa potentials, they do not describe dynamic electronic degrees of freedom. For the second set of simulations, we allow for explicit electronic degrees of freedom through the use of quantum-statistical potentials (QSPs) [81–83]. In particular, we employ a QSP composed of a diffractive term from Hansen–McDonald [81] and a Pauli exclusion term between electrons derived from the low-density limit of the spin-averaged Lado potential [82, 83]

$$u_{\alpha\gamma}^{\text{QS}}(r) = \frac{Z_\alpha Z_\gamma e^2}{r} (1 - e^{-r/\lambda_{\alpha\gamma}}) - \delta_{\alpha e} \delta_{\gamma e} T_e \ln \left(1 - \frac{1}{2} e^{-r^2/\pi\lambda_{ee}^2} \right),$$

where $\lambda_{\alpha\gamma} = \hbar / (2\pi\mu_{\alpha\gamma} T_{\alpha\gamma})^{1/2}$ is the thermal de Broglie wavelength, $\mu_{\alpha\gamma}$ is the reduced mass, and $\delta_{\alpha\gamma}$ is the Kronecker delta. Note that the indices (α, γ) now run over the electrons as well as the ions. Recent comparisons of the QSP model with PIMC predictions for radial distribution functions (RDFs) across a wide range of conditions [84] reveal the accuracy of QSPs for the conditions of PIPPs.

3.2. Atomic ionization model

Because we are considering compressed gases that are below solid density, we employ a non-ideal Saha equation rather than an average-atom model [74] to compute ionization levels. The framework of the Saha approach has the additional advantage that it naturally yields the distribution of charge states, not only the average. In its ideal form, the well-known Saha equations [75, 76] describing the transitions between N ionization states (in addition to the neutral state) are given by

$$\frac{n_{j+1}n_e}{n_j} = \frac{2g_{j+1}}{\lambda_{ee}^3 g_j} \exp\left(-\frac{E_j}{T_e}\right) \equiv f_{j+1}, \quad (6)$$

for $j \in [0, N-1]$, where $\{g_j\}$ are the statistical weights of the energy states, $\{E_j\}$ are the ionization energies, $\lambda_{ee} = \hbar / (2\pi m_e T_e)^{1/2}$ is the electron thermal de Broglie wavelength, and n_j is the number density of the j th ionization state. Finally, conservation of charge, $n_e = \sum_j j n_j$, and conservation of particle number, $n_i = \sum_j n_j$, result in a closed system of equations. To solve this system, we follow the approach of Zaghloul *et al* [77]. We can write (6) as a single equation in terms of the concentrations $x_j = n_j/n_i$ and the mean ionization $\langle Z \rangle = \sum_j j x_j$ as

$$\langle Z \rangle^{N+1} + \sum_{k=1}^N \left[n_i^{-k} (\langle Z \rangle - k) \langle Z \rangle^{N-k} \prod_{j=1}^k f_j \right] = 0. \quad (7)$$

A root solver can be used to solve for $\langle Z \rangle$, and once $\langle Z \rangle$ is known, the individual species concentrations can be calculated from the following recursion relations:

$$x_0 = \langle Z \rangle \left(\sum_{k=1}^N \frac{k}{n_i^k \langle Z \rangle^k} \prod_{j=1}^k f_j \right)^{-1}, \quad (8)$$

$$x_{j+1} = \left(\frac{f_{j+1}}{n_i \langle Z \rangle} \right) x_j. \quad (9)$$

For the specific case of Xe, we need to explore only the first few ionization states because of the limited temperature range of interest. Using the values obtained from [85], we take $N = 5$ and set $\{E_j\} = \{12, 21, 32, 46, 57\}$ eV. We estimate the statistical weights by assuming that Xe, like other noble gases (beyond He), initially ionizes by losing electrons from the outermost p -subshell. Taking values from [77, 86], we have $\{g_j\} = \{1, 6, 9, 4, 9, 6\}$. While the gas in consideration is below solid density, it is still compressed to form Xe–Xe correlations, and this basic Saha model must be extended to its non-ideal form to capture many-body screening effects.

In a dense plasma, the environment surrounding each atom can significantly modify the energy required for ionizing transitions. These modifications are collectively referred to as IPD because they tend to have the effect of lowering ionization energies. To capture the effects of IPD, we employ the standard method of Stewart and Pyatt (SP) [50]. While our choice of IPD model is not unique, we do not expect large deviations from the SP model and other IPD models in this regime. In the SP model, the electrostatic potential about a point ion is calculated using the following two assumptions:

- Within the ion-sphere radius ($r < a_i$), the ion density is zero, and the electron density is constant. (Here, a_i is the ion-sphere radius defined as $a_i = (3/4\pi n_i)^{1/3}$.)
- Beyond the ion-sphere radius ($r > a_i$), the electrons and ions exhibit linear screening in terms of their respective screening lengths.

Solving the associated Poisson equation and enforcing C^2 -continuity in the potential results in an electrostatic potential that can be radially expanded about an ion position as $u(r) \sim -Z_j e^2/r + \Delta E_j$, where ΔE_j is the IPD energy shift. This energy shift associated with the j th ionization state is given by

$$\Delta E_j = \frac{3Z_j e^2 \lambda_{\text{tot}}^2}{2a_i^3} \left[\left(\left(\frac{a_i}{\lambda_{\text{tot}}} \right)^3 + 1 \right)^{2/3} - 1 \right], \quad (10)$$

where $\lambda_{\text{tot}}^{-2} = \lambda_e^{-2} + \lambda_i^{-2}$. The ion screening length can be estimated using Debye–Hückel (DH) theory to obtain

$$\lambda_i^2 = \frac{T_i}{4\pi \langle Z \rangle^2 e^2 n_i}. \quad (11)$$

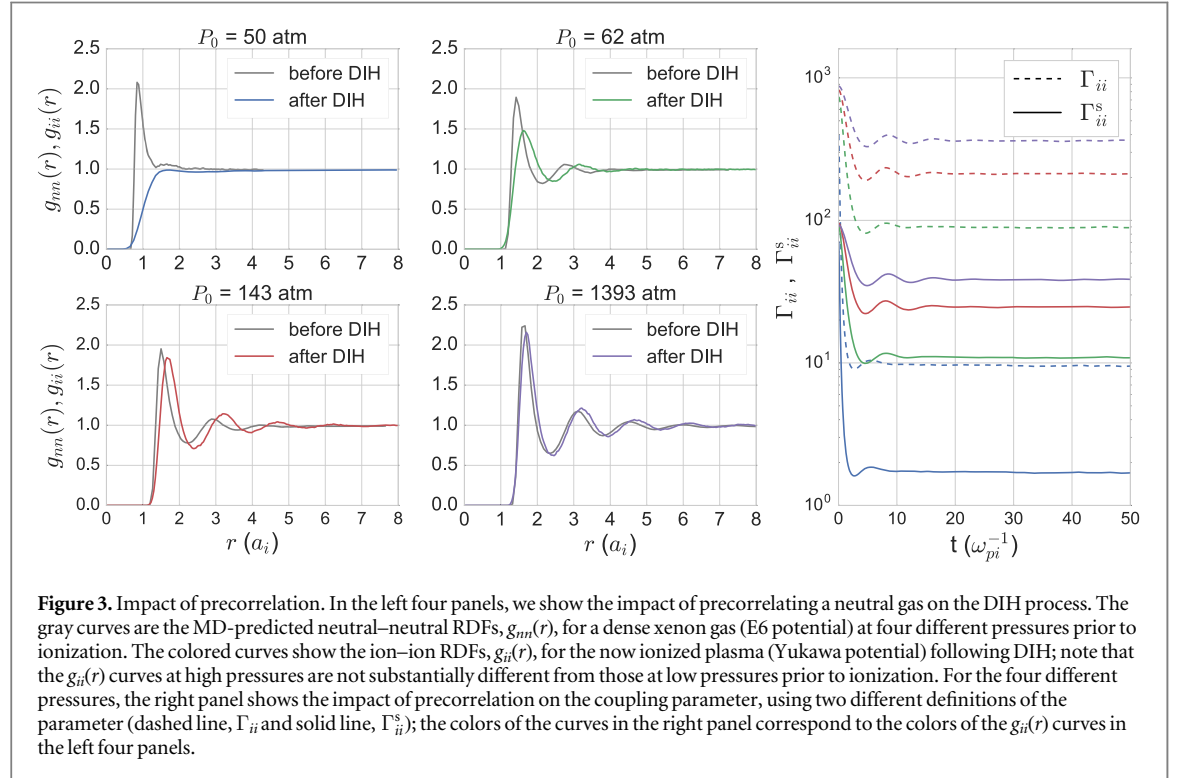
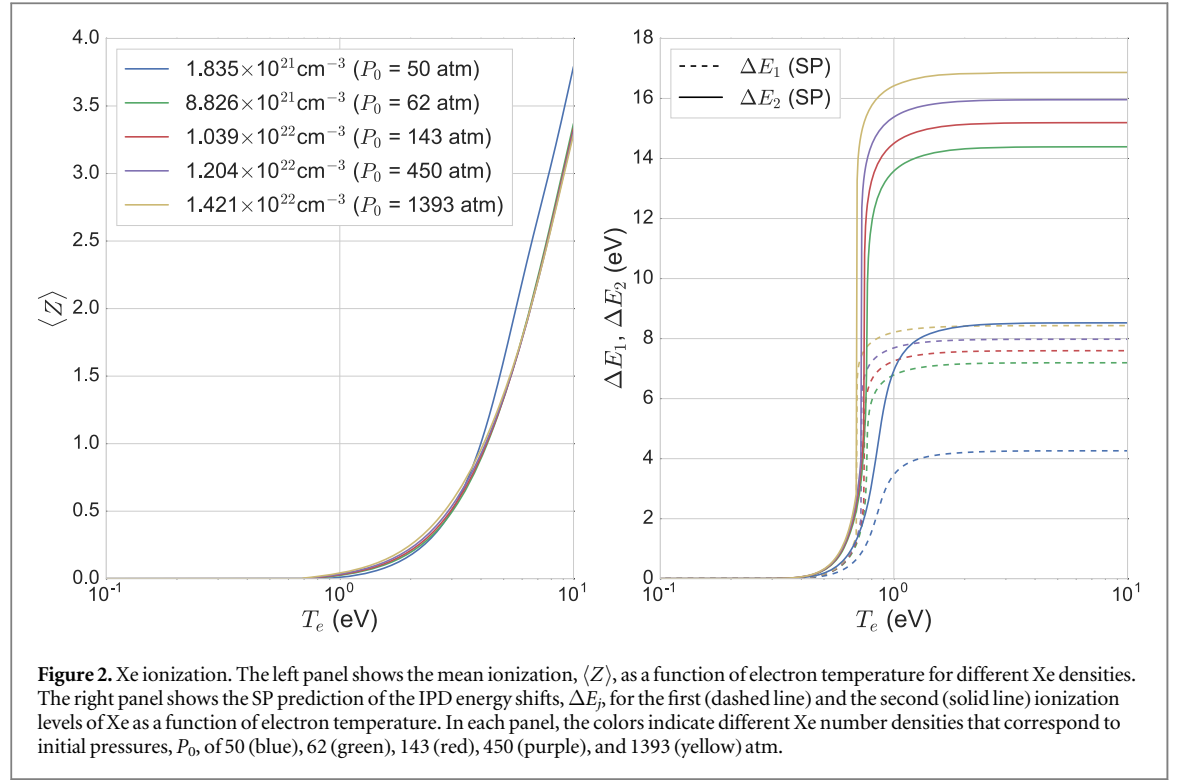
As in the Yukawa potential, we must additionally incorporate degeneracy via the Thomas–Fermi length. From this SP model, the energy levels are then shifted according to $\{E_j\} \rightarrow \{E_j - \Delta E_j\}$. The $\langle Z \rangle$ -dependence in the energy shifts transforms (7) from a polynomial to a transcendental equation.

Figure 2 shows $\langle Z \rangle$ and the energy shifts for the first (dashed) and second (solid) ionization levels of Xe, for densities corresponding to the initial pressures $P = \{50, 62, 143, 1393\}$ atm considered in section 4. The values of $\langle Z \rangle$ for pressures from 62 to 143 atm are similar for the range of T_e considered. This similarity arises because the corresponding densities are similar ($\sim 10^{22} \text{ cm}^{-3}$); however, the 50 atm case differs from the others for $T_e \gtrsim 4$ eV because of the lower densities for those cases ($\sim 10^{21} \text{ cm}^{-3}$). The corresponding energy-level shifts are shown in the right panel. The Yukawa potentials used in the MD simulations employ these ionization states and the screening length (5).

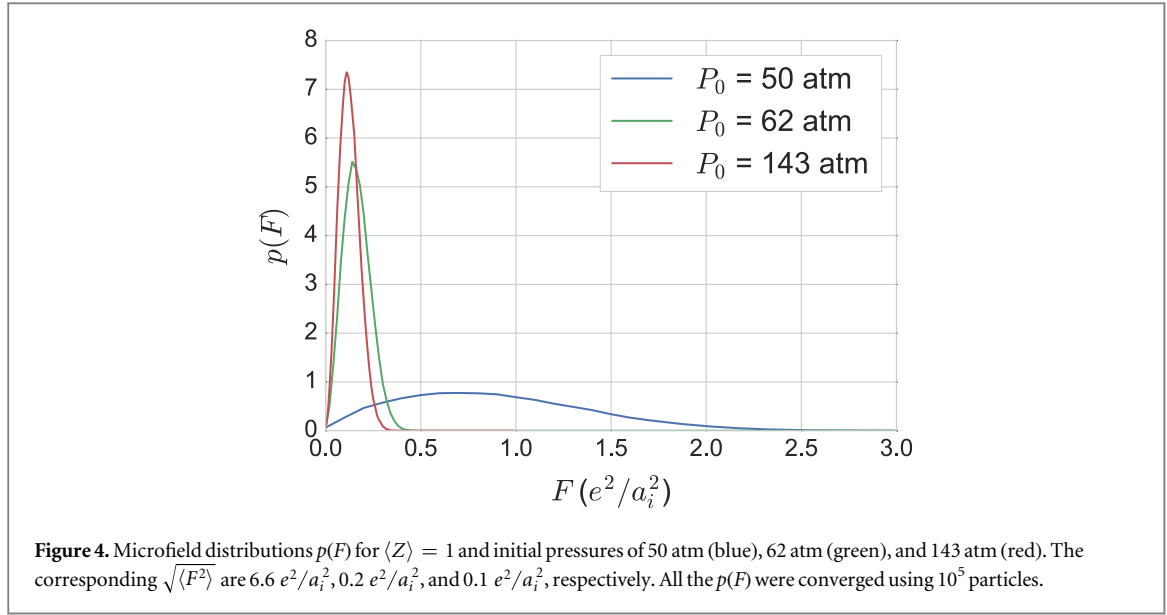
While it remains unclear which IPD model is most appropriate, we have employed this standard model both to self-consistently predict an accurate ionization state to use in the MD simulations and to illustrate the degree to which IPD physics can be explored with PIPPs. Our goal here is *not* to develop Saha models beyond this standard description. Future plasma experiments employing dense gases could provide more insights into IPD, and more refined models could then be developed.

4. Plasma properties in the PIPP regime

Before we examine how plasma properties vary across the PIPP and what this reveals about our knowledge of non-ideal plasmas, we demonstrate some features of precorrelation induced by pressure. Simulations were performed in which we first equilibrated the MD using the E6 potential and computed the RDF. Then, from those initial positions and velocities, we evolved the plasma to equilibrium using the Yukawa potential. Results for four different initial gas pressures $P_0 = \{50, 62, 143, 1393\}$ atm are shown in figure 3. In the left four panels, we show the initial (gray) neutral–neutral RDFs, $g_{nn}(r)$, and final (colored) ion–ion RDFs, $g_{ii}(r)$. It is evident that higher pressures result in increased correlation in the initial gas, which in turn leads to smaller differences in the RDF between the gas and plasma states. Thus, DIH can be controlled by varying the initial gas pressure, thereby allowing the Coulomb coupling of the resulting PIPP to be controlled.



While it is common to characterize non-ideal plasmas through the bare ionic Coulomb coupling parameter $\Gamma_{ii} = \langle Z \rangle^2 e^2 / a_i T_i$, PIPPs are two-temperature electron–ion mixtures that are not well characterized by Γ_{ii} . For this reason, an *effective* coupling parameter can be used to capture the coupling of the system more accurately. One such effective coupling parameter that approximates the effect of screening is given by $\Gamma_{ii}^s = \Gamma_{ii} e^{-\kappa}$ [87], where $\kappa = a_i / \lambda_e(T_e)$ is the screening parameter. The time evolution of these coupling parameters is shown in the right panel of figure 3, where $\langle Z \rangle = 2$ in each case. Over a range of initial gas pressures, the post-DIH Γ_{ii} ranges from roughly 10 to 364, which covers most of the strong-coupling regime. When screening is included via Γ_{ii}^s , effective couplings from roughly 1 to 40 are obtained, with κ varying from 1.7 to 2.2 (see figure 6). Thus,



PIPPs can be used to create much larger variations in the effective coupling strength than can their UCNP counterparts [62, 79].

To better understand why such a steep transition takes place as the initial pressure goes from 50 to 62 atm, we examine the underlying microfields of the plasma after photoionization. We introduce the microfield distribution

$$p(F) = 4\pi F^2 \left\langle \sum_{j=1}^N \delta(\mathbf{F} - \mathbf{F}_j(0)) \right\rangle, \quad (12)$$

which represents the distribution of forces \mathbf{F} (in units of e^2/a_i^2) on the initial energy landscape of the system immediately after ionization; here N is the number of ions in the system, $\mathbf{F}_j(0)$ is the net force on the j th ion at $t = 0$, where $t = 0$ marks the instant of ionization, and $\langle \rangle$ denotes the ensemble average. Following the analysis of [42], the early-time temperature evolution can be described as $\tilde{T}(t) \approx \tilde{T}(0) + (t/\tau_2)^2$, where \tilde{T} is the temperature in units of e^2/a_i , t is time in units of inverse plasma frequency ω_p^{-1} , $\tau_2 = 3/\sqrt{\langle F^2 \rangle}$, and $\langle F^2 \rangle = \int dF F^2 p(F)$.

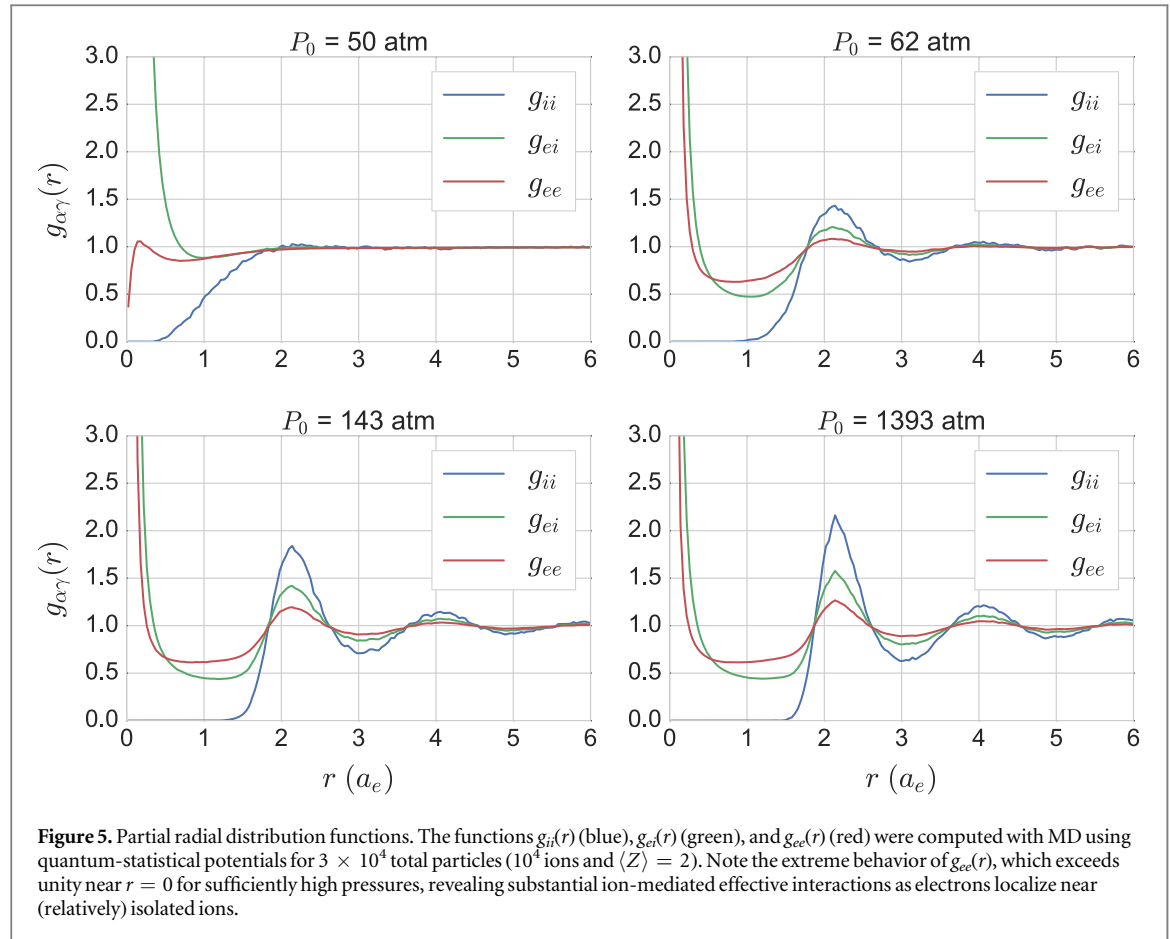
We can process our MD data to obtain microfields immediately after ionization of the correlated gas. Figure 4 shows $p(F)$ for $\langle Z \rangle = 1$ and initial pressures of 50, 62 and 143 atm; all $p(F)$ were converged using 10^5 particles. As the initial pressure is increased from 50 to 143 atm, the peak of $p(F)$ shifts towards smaller F , and the width of $p(F)$ decreases, thereby decreasing $\langle F^2 \rangle$ from $\sim 6.6 e^2/a_i^2$ to $\sim 0.1 e^2/a_i^2$. This shift in the microfield distribution peak to a lower value of F indicates far more cancellations in the interparticle forces. Further, the most significant changes in $p(F)$ occur from 50 to 62 atm, which could be attributed to a Fisher–Widom or Kirkwood line crossing, as suggested by the change in the RDFs from monotonic to oscillatory in figure 3³.

Having established that DIH can be partly mitigated in a controlled manner to achieve a range of coupling strengths, we turn to some of the unique plasma properties that can be measured with PIPPs. For these studies, we include the electronic degrees of freedom explicitly in the MD simulations through the use of QSPs for a more complete exploration of the relevant physics.

4.1. Strong electron–ion coupling

We begin by examining the intraspecies correlation functions $g_{ii}(r)$, $g_{ei}(r)$ and $g_{ee}(r)$, which are shown in figure 5 for four different initial gas pressures; the RDFs are at the post-DIH temperature. There are some interesting features in the RDFs that merit a brief discussion. The electron–electron RDF undergoes a Kirkwood-like transition in the region near 50 atm, with its peak at the same location as the ion peak; there are strong correlations in the peak locations of $g_{ei}(r)$ and $g_{ee}(r)$ with those of $g_{ii}(r)$, suggesting that the electrons are highly localized around the ions in these plasmas. Moreover, $g_{ee}(0) > 1$ for most of the initial gas pressures considered, indicating that an effective attraction between electrons (mediated by the ions) exists.

³ While the monotonic-oscillatory crossover is similar in both the Kirkwood and Widom–Fisher cases, [89] gives a precise distinction based on the structure of the poles of the correlation functions. We did not perform such an analysis here and therefore do not know which type of line we have; we leave that analysis for future work.



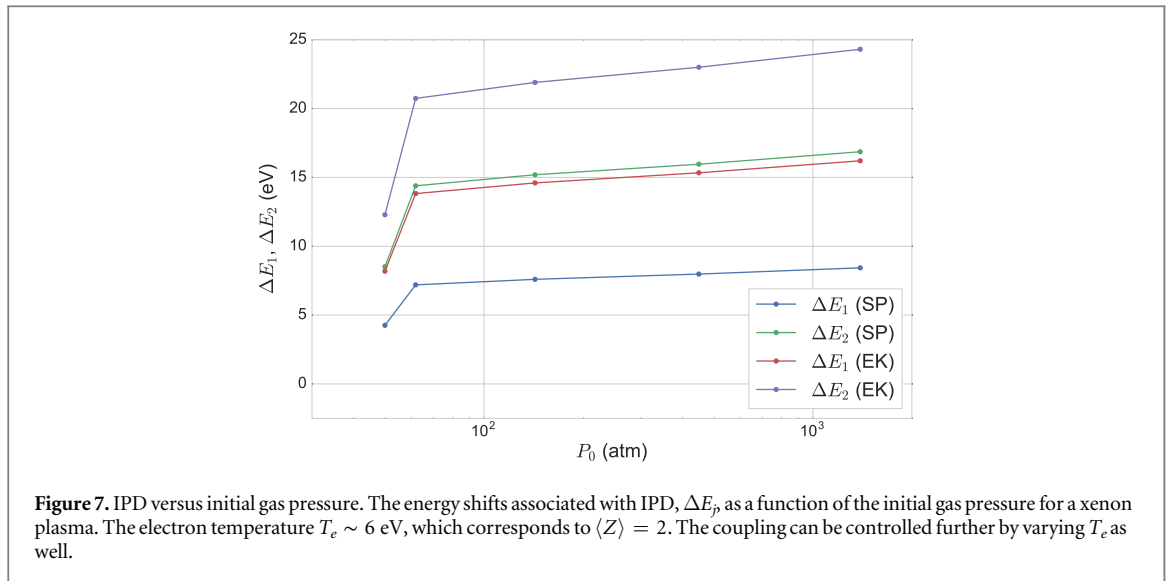
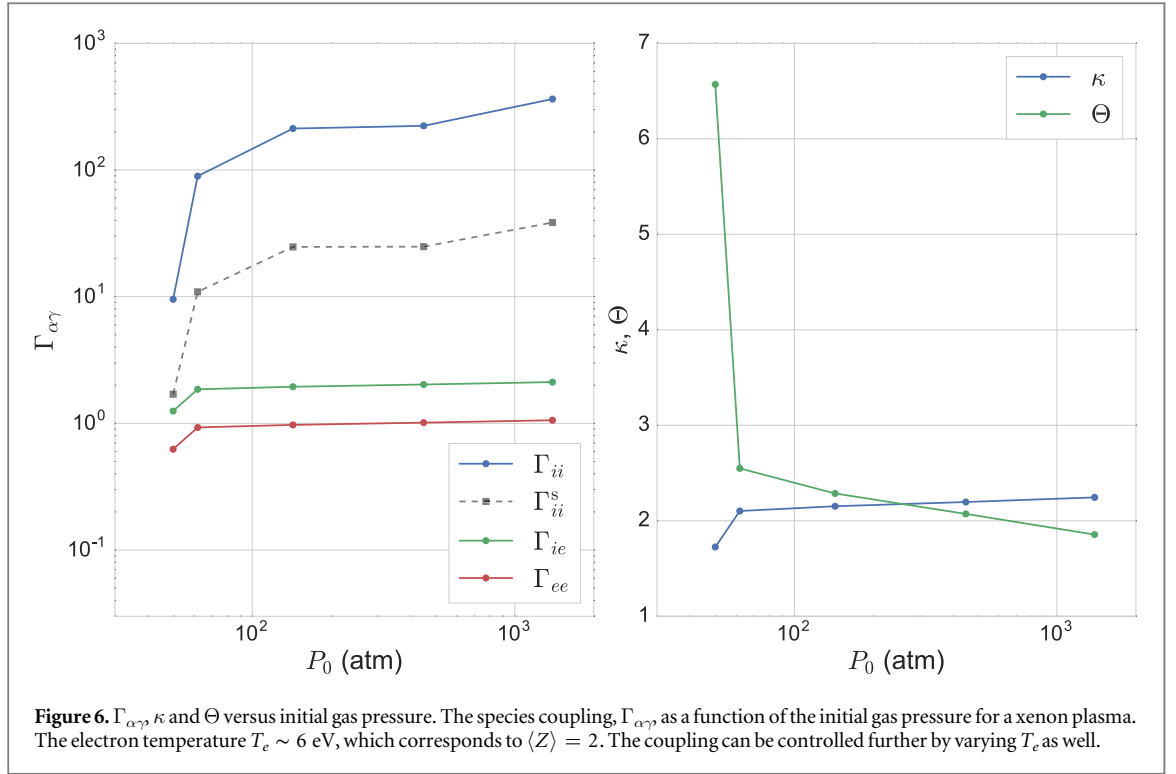
From these simulations, several simple plasmas properties can be immediately examined. In particular, we can calculate the explicit coupling between the ions and electrons through an interspecies coupling parameter $\Gamma_{\alpha\gamma} = |Z_\alpha Z_\gamma e^2|/a_{\alpha\gamma} T_{\alpha\gamma}$, where $T_{\alpha\gamma} = (m_\alpha T_\gamma + m_\gamma T_\alpha)/(m_\alpha + m_\gamma)$ [88], species masses are m_α and m_γ , the ion-sphere radius is $a_{ii} = a_i$ and the electron-sphere radius is $a_{ee} = a_{ei} = a_e = (3/4\pi n_e)^{1/3}$. We can additionally examine the screening strength $\kappa = a_i/\lambda_e$ and degeneracy parameter $\Theta = T_e/E_F$. Species couplings $\Gamma_{\alpha\gamma}$ are shown in the left panel of figure 6, where we see that the largest variations in the species couplings occur in the 50–100 atm range. The coupling strength and degeneracy are shown in the right panel of figure 6, and while the screening parameter remained approximately constant, the degeneracy varied by a factor of more than three. We have also explored the more complex plasma properties of (1) IPD, (2) transport phenomena, and (3) EOS, which we have described in detail below.

4.2. Ionization potential depression

IPD has seen renewed interest recently in the context of dense plasma experiments [53, 55]. The energy shifts associated with IPD modify the ionization balance in a plasma, and this balance affects important properties such as opacity, the EOS, and transport coefficients. Further, these modifications to the ionization balance become more pronounced as the coupling increases. Despite the significance of IPD physics, there is a lack of well-established models that describe the phenomenon, as has been shown by recent dense plasma experiments [55]. The widely used SP model of IPD was found to increasingly disagree with measurements in these dense plasma experiments at higher ionization levels (see section 3.2 for a review of the SP model). Instead, the lesser-known Ecker–Kröll model, given by

$$\Delta E_j = (Z_j + 1)(\langle Z \rangle + 1)^{1/3} \left(\frac{e^2}{a_i} \right) \quad (13)$$

for the j th ionization state [51], offered better agreement with IPD measurements for the same conditions. As shown in figure 7, the significant differences between the SP and Ecker–Kröll predictions of IPD for PIPP conditions are similar to those observed in dense plasma experiments. Thus, the lower energy-density environments of PIPPs (relative to dense plasmas) and their controllability over a range of densities enable these plasmas to provide an optimal platform for validating different IPD models without the complexities associated with dense plasma conditions.



A notable feature in the IPD predictions is the sensitivity to pressure in the 50–62 atm range, a property shared with the other applications discussed below. Re-examining figure 3, we see that the gas RDF undergoes a monotonic-oscillatory transition, which is either a Kirkwood or Fisher–Widom transition [89]; this transition can be seen in particular in the 50–62 atm range (blue and green curves). Thus, establishing the Kirkwood/Fisher–Widom line for the gas of interest can yield considerable controllability.

4.3. Transport phenomena

Turning next to transport phenomena, which are critical to a hydrodynamic description of plasmas, PIPPs can provide a platform for exploring quantities such as transport coefficients (diffusivities, viscosities, conductivities, etc) that are relevant to conditions in ICF experiments [45, 57, 58, 74]. Most transport coefficients tend to be inversely proportional (or proportional) to a scattering cross section, which generally is not a transferable quantity among different transport processes [74]; however, we can explore the qualitative effects of variations in PIPP conditions on these cross sections by employing a Coulomb logarithm (CL) as a proxy. Here, we consider CLs of the form [74]

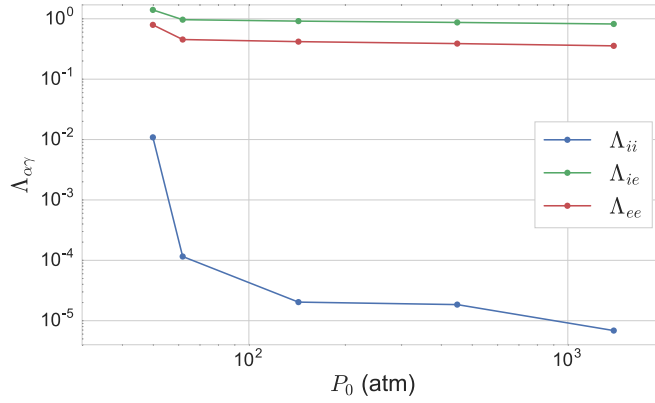


Figure 8. $\Lambda_{\alpha\gamma}$ versus initial gas pressure. The Coulomb logarithm, $\Lambda_{\alpha\gamma}$, as a function of the initial gas pressure for a xenon plasma. The electron temperature $T_e \sim 6$ eV, which corresponds to $\langle Z \rangle = 2$. The coupling can be controlled further by varying T_e as well.

$$\Lambda_{\alpha\gamma} = \frac{1}{2} \ln \left(1 + \left(\frac{b_{\alpha\gamma}^{\max}}{b_{\alpha\gamma}^{\min}} \right)^2 \right), \quad (14)$$

where the minimum impact parameter is given by $b_{\alpha\gamma}^{\min} = |Z_\alpha Z_\gamma| e^2 / (2T_{\alpha\gamma})$, and the maximum impact parameters are given by $b_{ii}^{\max} = ((\lambda_i^2 + a_i^2)^{-1} + (\lambda_e^2 + a_e^2)^{-1})^{-1/2}$ and $b_{ee}^{\max} = b_{ei}^{\max} = (\lambda_e^2 + a_e^2)^{1/2}$, with $\lambda_i = (T_i / (4\pi n_i \langle Z \rangle^2 e^2))^{1/2}$ being the ionic screening length. This form is used to yield more physically relevant results in the strongly coupled regime, as the more common form $\ln(b_{\alpha\gamma}^{\max}/b_{\alpha\gamma}^{\min})$ is, in fact, negative in this regime. CLs are presented in figure 8, where order-of-magnitude variations are seen in Λ_{ii} . Note that all three CLs are near unity or smaller, representing the most theoretically challenging regime of transport in plasmas.

4.4. Equation of state

Finally, we examine PIPPs as a platform for investigating multi-temperature EOS models, which are essential to the hydrodynamic description of a plasma [90]. For example, large-scale experiments involving plasmas (e.g., ICF) require an accurate EOS for their design and interpretation [56, 57, 91, 92]. Because electrons and ions are at different temperatures in most laboratory plasmas, it is important to develop an accurate two-temperature EOS. Although theoretical efforts have explored this topic over many years [88, 93–96], much less experimental work on this subject has been conducted. To understand the role that PIPPs could play in such experimental studies, we calculate final system pressures using MD simulations as the initial pressure of the gas phase is varied.

Here, we present a two-temperature generalization for comparison with MD simulations. The total pressure of a multi-component system can be decomposed as

$$P = \sum_{\alpha} P_{\alpha}^0 + \sum_{\alpha,\gamma} P_{\alpha\gamma}^{\text{ex}}, \quad (15)$$

$$P_{\alpha\gamma}^{\text{ex}} = -\frac{n_{\alpha} n_{\gamma}}{6} \int d\mathbf{r} \, r \frac{du_{\alpha\gamma}}{dr} g_{\alpha\gamma}(r), \quad (16)$$

where $P_{\alpha}^0 = n_{\alpha} T_{\alpha}$ are the ideal pressures. For long-range interactions such as QSPs (i.e., interactions that scale as $1/r$ for large r), the excess pressures $P_{\alpha\gamma}^{\text{ex}}$ are individually divergent due to the interaction with the uniform background. It is thus useful to introduce the *total* correlation functions $h_{\alpha\gamma}(r) = g_{\alpha\gamma}(r) - 1$, which allow the uniform background contributions to cancel, and the change in excess pressures can instead be expressed in terms of the finite expressions

$$\Delta P_{\alpha\gamma}^{\text{ex}} = -\frac{n_{\alpha} n_{\gamma}}{6} \int d\mathbf{r} \, r \frac{du_{\alpha\gamma}}{dr} h_{\alpha\gamma}(r). \quad (17)$$

These total correlation functions are connected to the *direct* correlation functions $c_{ij}(r)$ through the multicomponent Ornstein–Zernike equations, which, in Fourier space, are given by

$$h_{\alpha\gamma}(k) = c_{\alpha\gamma}(k) + \sum_l n_l c_{\alpha l}(k) h_{l\gamma}(k). \quad (18)$$

Partial pressures calculated from the MD simulations are shown in the left panel of figure 9 in units of the ideal-electron pressure. Here, the electron–ion contribution to the excess pressure is shown to vary the most, and this finding could be of interest for experiments focused on electron–ion interactions. However, the *total* pressure, which is primarily dominated by the ideal-electron pressure, is of the most interest from a hydrodynamic perspective.

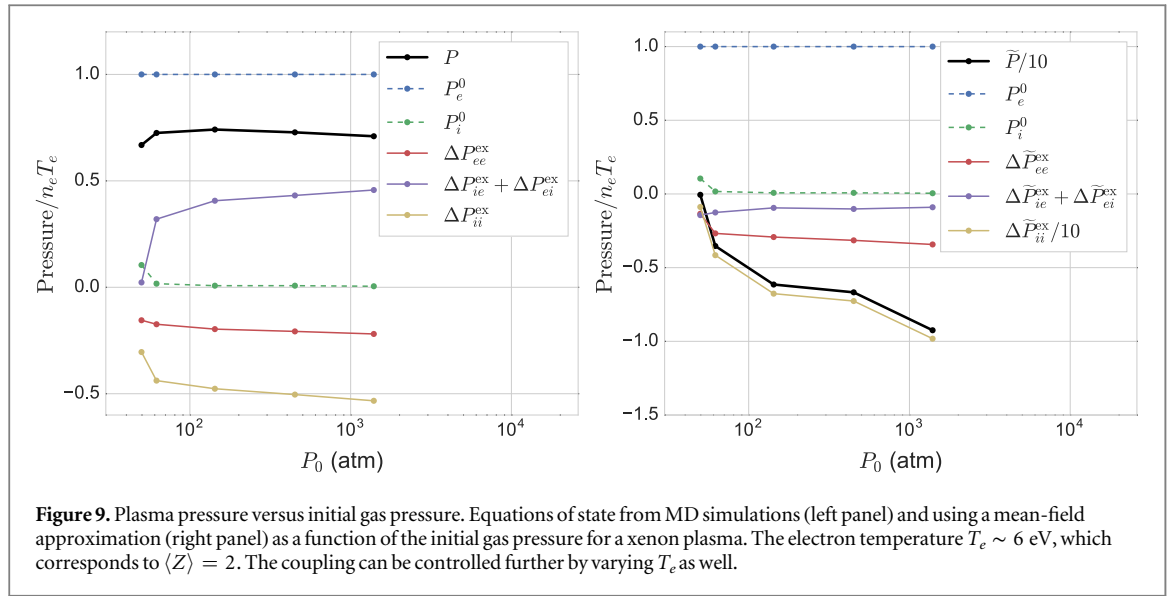


Figure 9. Plasma pressure versus initial gas pressure. Equations of state from MD simulations (left panel) and using a mean-field approximation (right panel) as a function of the initial gas pressure for a xenon plasma. The electron temperature $T_e \sim 6$ eV, which corresponds to $\langle Z \rangle = 2$. The coupling can be controlled further by varying T_e as well.

For comparison, we employ DH theory, which is commonly used to describe a number of plasma properties [60, 61, 97] due to its analytic simplicity. The DH limit is defined here by approximating the direct correlation functions in terms of the inter-particle interactions as $c_{ij}(r) \approx -\beta_{ij} u_{ij}(r)$, where $\beta_{\alpha\gamma} = 1/T_{\alpha\gamma}$ is the inverse of the mass-weighted cross temperature (in energy units) given by $T_{\alpha\gamma} = (m_\alpha T_\gamma + m_\gamma T_\alpha)/(m_\alpha + m_\gamma)$ [88]. This approximation, which is valid in the weakly-coupled limit, often yields convenient closed-form solutions for many quantities of interest, leading to its wide use. However, as is well known, DH theory fails above modest coupling. Abe has given the leading-order corrections to the DH approximation [98], which have been verified by Monte Carlo simulations [99], but less is known about the two-temperature case. Additionally, few experiments span the region over which the DH limit is accurate to the region over which Abe-like corrections become important and then fail themselves. PIPPs thus provide a natural platform for exploring all of these issues.

While using the QSPs as the interaction within the DH approximation would be a more consistent choice for comparison to the MD simulations, spurious results arise due to the multi-temperature nature of the calculation. For this reason, we instead choose the interaction to be the simpler Coulomb potential, $u_{\alpha\gamma}(r) = Z_\alpha Z_\gamma e^2/r$, and thus the change in excess pressures can be expressed as

$$\Delta \tilde{P}_{\alpha\gamma}^{\text{ex}} = \frac{1}{6} Z_\alpha Z_\gamma n_\alpha n_\gamma \int dr \left(\frac{e^2}{r} \right) h_{\alpha\gamma}(r) \quad (19)$$

$$= \frac{1}{6} Z_\alpha Z_\gamma n_\alpha n_\gamma \int \frac{dk}{(2\pi)^3} v(k) h_{\alpha\gamma}(k) \quad (20)$$

$$= \frac{1}{3\pi} Z_\alpha Z_\gamma e^2 n_\alpha n_\gamma \int_0^\infty dk h_{\alpha\gamma}(k). \quad (21)$$

Here, the two components are the ions (i) and the electrons (e), with $Z_i = \langle Z \rangle$, $Z_e = -1$, and $n_e = \langle Z \rangle n_i$, and we have used a tilde (\sim) to denote pressures calculated within the DH approximation. Using the Ornstein–Zernike equations (18), the total correlation functions can then be calculated as

$$h_{ii} = \frac{1}{D} [n_e \phi_{ie}^2 - (1 + n_e \phi_{ee}) \phi_{ii}], \quad (22)$$

$$h_{ee} = \frac{1}{D} [n_i \phi_{ie}^2 - (1 + n_i \phi_{ii}) \phi_{ee}], \quad (23)$$

$$h_{ie} = -\frac{1}{D} \phi_{ie}, \quad (24)$$

$$D \equiv (1 + n_i \phi_{ii})(1 + n_e \phi_{ee}) - n_i n_e \phi_{ie}^2, \quad (25)$$

where we have introduced the function $\phi_{\alpha\gamma}(k) = 4\pi\beta_{\alpha\gamma} Z_\alpha Z_\gamma e^2/k^2$. We can then substitute these relations into (21) to obtain

$$\Delta \tilde{P}_{ii}^{\text{ex}} = -\frac{2\pi \langle Z \rangle^4 e^4 n_i^2}{3(k_+ + k_-)} \left(\beta_i + \frac{4\pi e^2 \langle Z \rangle n_i B}{k_- k_+} \right), \quad (26)$$

$$\Delta\tilde{P}_{ie}^{\text{ex}} = \Delta\tilde{P}_{ei}^{\text{ex}} = -\frac{2\pi\langle Z\rangle^3 e^4 n_i^2 \beta_{ie}}{3(k_+ + k_-)}, \quad (27)$$

$$B \equiv \beta_i \beta_e - \beta_{ie}^2, \quad (28)$$

where the roots k_{\pm} are defined as

$$k_{\pm}^2 = 2\pi e^2 \langle Z \rangle n_i [\beta_e + \langle Z \rangle \beta_i \pm \sqrt{(\beta_e - \langle Z \rangle \beta_i)^2 + 4\langle Z \rangle \beta_{ie}^2}]. \quad (29)$$

It should be noted that k_{\pm}^2 is always real; however, the root k_-^2 becomes negative for $B < 0$, which leads to an unphysical result for the correlation functions and consequently the pressures. Given our definition of T_{ij} , this spurious range is encountered for the temperature ratios $(m_e/m_i)^2 < T_e/T_i < 1$, where we have assumed that $m_e < m_i$. However, $T_e \gg T_i$ for our systems of interest, hence this regime will be avoided naturally. Finally, the total pressure is given by

$$P = n_i T_i + \langle Z \rangle n_i T_e + \Delta\tilde{P}_{\text{tot}}^{\text{ex}}, \quad (30)$$

$$\Delta\tilde{P}_{\text{tot}}^{\text{ex}} = -\frac{2\pi\langle Z\rangle^2 e^4 n_i^2}{3(k_+ + k_-)} \left[\beta_i \langle Z \rangle^2 + 2\langle Z \rangle \beta_{ie} + \beta_e + 4\pi\langle Z \rangle^2 (\langle Z \rangle + 1) \frac{e^2 n_i B}{k_+ k_-} \right]. \quad (31)$$

In the single-temperature limit, where the temperature ratio is unity, many of the above quantities simplify dramatically. Here, we have $\beta = \beta_e = \beta_i = \beta_{ie}$, and the correlation functions can be expressed as

$$h_{\alpha\gamma}(k) = \frac{-Z_{\alpha} Z_{\gamma} \beta v(k)}{1 + n_i \langle Z \rangle (\langle Z \rangle + 1) \beta v(k)}. \quad (32)$$

The total excess pressure reduces to

$$\Delta\tilde{P}_{\text{tot}}^{\text{ex}} = -\frac{T}{24\pi\lambda_{\text{DH}}^3}, \quad (33)$$

$$\lambda_{\text{DH}} = [4\pi\langle Z \rangle e^2 n_i \beta (1 + \langle Z \rangle)]^{-1/2}, \quad (34)$$

which is the standard DH result. Similarly, in the limit $T_e \gg T_i$, the leading-order excess pressure is given by the ion–ion correlations in the form $\Delta\tilde{P}_{\text{tot}}^{\text{ex}} \sim -T_i/(24\pi\lambda_i^3)$, where $\lambda_i = (4\pi\langle Z \rangle^2 e^2 n_i \beta_i)^{-1/2}$.

The DH results provide useful formulae for estimating various quantities. Moreover, since it is well-known that the DH approximation fails for non-ideal plasmas, we use it to compare with the more accurate models to suggest which experiments are in regions beyond what DH is capable of describing. For example, as shown in the right panel of figure 9, the two methods predict total pressures with the opposite sign and disparate magnitudes. Note that we have reduced both \tilde{P} and $\Delta\tilde{P}_{ii}^{\text{ex}}$ by a factor of 10 to clearly show the variations in the other partial pressures. A striking observation is that the total pressure predicted by DH is negative in all cases because of the contribution of the ion–ion excess pressure. Moreover, the electron–ion excess pressure has a sign opposite that of its MD analog. These observations lead us to conclude that the DH approximation severely breaks down for the PIPP conditions studied here. Such disparities between the DH and MD predictions call for validation of the different EOS models with experiments.

5. Summary, conclusion and outlook

In summary, we have proposed a strategy for creating non-ideal plasmas at densities intermediate to UCNPs and dense plasmas. Because these plasmas mitigate DIH through correlations induced by pressure, we refer to them as PIPPs. We have studied PIPPs through a series of MD simulations that simulate the neutral gas before ionization to establish neutral–neutral correlations. From those initial states, we further evolve the system in the plasma state to examine the impact of those correlations. We discovered that there is a narrow pressure range over which there is a transition from weak to strong DIH mitigation, and we have identified that with a Fisher–Widom or Kirkwood line in the neutral gas. We anticipate that PIPPs can exploit this behavior to create a platform that allows for unique variations in plasma properties without some of the complexities of UCNPs and dense plasmas, which perhaps allows for diagnostics such as near-visible Thomson scattering and terahertz spectroscopy [100–104] to be developed for non-ideal plasmas. Importantly, this behavior occurs near conditions of previous experiments [60, 61].

We have quantified the potential range of coupling parameters that PIPPs might explore, using both bare and screened coupling parameters. We found, as shown in the left panel of figure 6, that the post-DIH Γ_{ii} varies from roughly 10 to 364, which covers most of the strong-coupling regime. When the effect of screening is included, the effective coupling Γ_{ii}^s varies from roughly 1 to 40. These predictions suggest much larger couplings than can be achieved by UCNPs. Through simulation studies with explicit electrons, we have also shown that novel strong coupling behavior among the electrons may be achievable with PIPPs. In particular, our results

indicate that an effective *attractive* interaction between electrons can be created in this intermediate density regime. This attraction, revealed through studies of $g_{ee}(r)$ in which $g_{ee}(0) > 1$, is mitigated by strong electron–ion coupling. Because PIPPs allow for a wide range of electron temperatures, depending on the ionization laser energy, electron attraction is potentially very precisely controllable in PIPPs.

We also examined variations of a number of other quantities, including IPD and transport phenomena (using the CL as a generic proxy). IPD predictions for PIPPs using the SP and EK model (see figure 7) shows differences that are similar to the differences between the predictions of the two models observed in dense plasma experiments. Thus, the lower energy-density environments and their controllability over a range of densities enable these plasmas to provide an optimal platform for validating different IPD models without the complexities associated with dense plasma conditions. Figure 8 shows our predictions for ion–ion, ion–electron and electron–electron CLs; all are near unity or smaller, representing the most theoretically challenging regime of transport in plasmas; in particular, the ion–ion CL shows a three order-of-magnitude variation over the range of initial gas pressures considered.

We performed a careful study of two-temperature EOS using MD with electrons simulated explicitly using QSPs; the MD predictions of two-temperature EOS were then compared with the EOS predicted by a two-temperature DH theory (see figure 9). The EOS predicted by DH theory differs significantly from the MD prediction of EOS, both in magnitude and sign, suggesting not only that PIPPs explore EOS regimes of interest, but also that experimental design studies cannot rely on DH theory. As an aside, our studies have also revealed the drastic failure of the two-temperature DH theory and motivate the need for more theoretical work on two-temperature equations of state.

There are many avenues for future work based on these studies. From a modeling point of view, the potentials could be improved to allow for more accuracy across larger ranges of pressure. Moreover, the models could be extended to elements other than Xe and to mixtures, perhaps involving molecules. With better models, and more species, interesting regimes of PIPPs could be better identified and used to motivate specific experiments. Our results also point to theoretical issues that require further development, such as CLs near zero and two-temperature equations of state. So far, we have not explored non-steady-state properties of PIPPs, or whether they can be sculpted or tagged [34, 36]. Most importantly, future work is needed to explore realistic experimental designs, and explore how a wider array of diagnostics might be included in these non-ideal plasma studies.

Acknowledgments

The authors would like to thank Lisa Murillo for her detailed editing of the document. The work of Dharuman and Murillo was supported by the Air Force Office of Scientific Research (Grant No. FA9550-17-1-0394).

References

- [1] Benage J F Jr, Shanahan W R, Sherwood E G, Jones L A and Trainor R J 1994 Measurement of the electrical resistivity of a dense strongly coupled plasma *Phys. Rev. E* **49** 4391
- [2] DeSilva A W and Katsouros J D 1998 Electrical conductivity of dense copper and aluminum plasmas *Phys. Rev. E* **57** 5945
- [3] Grinenko A, Gurovich V T, Saypin A, Efimov S, Krasik Y E and Oreshkin V I 2005 Strongly coupled copper plasma generated by underwater electrical wire explosion *Phys. Rev. E* **72** 066401
- [4] Brown E F 2000 Nuclear heating and melted layers in the inner crust of an accreting neutron star *Astrophys. J.* **531** 988
- [5] Bildsten L and Hall D M 2001 Gravitational settling of ^{22}Ne in liquid white dwarf interiors *Astrophys. J.* **549** L219
- [6] Brown E F, Bildsten L and Chang P 2002 Variability in the thermal emission from accreting neutron star transients *Astrophys. J.* **574** 920
- [7] Peng F, Brown E F and Truran J W 2007 Sedimentation and type I x-ray bursts at low accretion rates *Astrophys. J.* **654** 1022
- [8] Hughto J, Schneider A S, Horowitz C J and Berry D K 2010 Diffusion of neon in white dwarf stars *Phys. Rev. E* **82** 066401
- [9] Fortney J J and Nettelmann N 2010 The interior structure, composition, and evolution of giant planets *Space Sci. Rev.* **152** 423
- [10] Vinko S M et al 2012 Creation and diagnosis of a solid-density plasma with an x-ray free-electron laser *Nature* **482** 59
- [11] Sperling P et al 2015 Free-electron x-ray laser measurements of collisional-damped plasmons in isochorically heated warm dense matter *Phys. Rev. Lett.* **115** 115001
- [12] Fletcher L B et al 2015 Ultrabright x-ray laser scattering for dynamic warm dense matter physics *Nat. Photon.* **9** 274
- [13] Glenzer S H et al 2016 Matter under extreme conditions experiments at the Linac Coherent Light Source *J. Phys. B: At. Mol. Opt. Phys.* **49** 092001
- [14] Plasma Science Committee 2003 *Frontiers in High Energy Density Physics: The X-Games of Contemporary Science* (Washington, DC: National Academies Press)
- [15] Thomas H, Morfill G, Demmel V, Goree J, Feuerbacher B and Möhlmann D 1994 Plasma crystal: Coulomb crystallization in a dusty plasma *Phys. Rev. Lett.* **72** 652
- [16] Pieper J B and Goree J 1996 Dispersion of plasma dust acoustic waves in the strong coupling regime *Phys. Rev. Lett.* **77** 3137
- [17] Nosenko V and Goree J 2004 Shear flows and shear viscosity in a two-dimensional Yukawa system (dusty plasma) *Phys. Rev. Lett.* **93** 155004
- [18] Nosenko V, Zhdanov S, Ivlev A, Morfill G, Goree J and Piel A 2008 Heat transport in a two-dimensional complex (dusty) plasma at melting conditions *Phys. Rev. Lett.* **100** 025003

- [19] Tsai Y Y, Tsai J Y and Lin I 2016 Generation of acoustic rogue waves in dusty plasmas through three-dimensional particle focusing by distorted waveforms *Nat. Phys.* **12** 573
- [20] Haralson Z and Goree J 2017 Overestimation of viscosity by the Green–Kubo method in a dusty plasma experiment *Phys. Rev. Lett.* **118** 195001
- [21] Grimes C C and Adams G 1979 Evidence for a liquid-to-crystal phase transition in a classical, two-dimensional sheet of electrons *Phys. Rev. Lett.* **42** 795
- [22] Fisher D S, Halperin B I and Platzman P M 1979 Phonon-rippion coupling and the two-dimensional electron solid on a liquid-helium surface *Phys. Rev. Lett.* **42** 798
- [23] Totsuji H 2012 Conduction of strongly coupled electrons through narrow channels on liquid helium surface: simulation *Contrib. Plasma Phys.* **52** 74
- [24] Mitchell T B, Bollinger J J, Dubin D H E, Huang X-P, Itano W M and Baughman R H 1998 Direct observations of structural phase transitions in planar crystallized ion plasmas *Science* **282** 1290
- [25] Jensen M J, Hasegawa T, Bollinger J J and Dubin D H E 2005 Rapid heating of a strongly coupled plasma near the solid–liquid phase transition *Phys. Rev. Lett.* **94** 025001
- [26] Dubin D H E 2005 Measurement of screening enhancement to nuclear reaction rates using a strongly magnetized and strongly correlated non-neutral plasma *Phys. Rev. Lett.* **94** 025002
- [27] Anderegg F, Dubin D H E, O’Neil T M and Driscoll C F 2009 Measurement of correlation-enhanced collision rates *Phys. Rev. Lett.* **102** 185001
- [28] Killian T C, Kulin S, Bergeson S D, Orozco L A, Orzel C and Rolston S L 1999 Creation of an ultracold neutral plasma *Phys. Rev. Lett.* **83** 4776
- [29] Kulin S, Killian T C, Bergeson S D and Rolston S L 2000 Plasma oscillations and expansion of an ultracold neutral plasma *Phys. Rev. Lett.* **85** 318
- [30] Simien C E, Chen Y C, Gupta P, Laha S, Martinez Y N, Mickelson P G, Nagel S B and Killian T C 2004 Using absorption imaging to study ion dynamics in an ultracold neutral plasma *Phys. Rev. Lett.* **92** 143001
- [31] Chen Y C, Simien C E, Gupta P, Laha S, Martinez Y N, Mickelson P G, Nagel S B and Killian T C 2004 Electron screening and kinetic energy oscillations in a strongly coupled plasma *Phys. Rev. Lett.* **93** 265003
- [32] Gupta P, Laha S, Simien C E, Gao H, Castro J, Killian T C and Pohl T 2007 Electron temperature evolution in expanding ultracold neutral plasmas *Phys. Rev. Lett.* **99** 075005
- [33] Killian T C 2007 Ultracold neutral plasmas *Science* **316** 705
- [34] Castro J, McQuillen P and Killian T C 2010 Ion acoustic waves in ultracold neutral plasmas *Phys. Rev. Lett.* **105** 065004
- [35] Heilmann N, Peatross J B and Bergeson S D 2012 Ultracold neutral plasmas at room temperature *Phys. Rev. Lett.* **109** 035002
- [36] Bannasch G, Castro J, McQuillen P, Pohl T and Killian T C 2012 Velocity relaxation in a strongly coupled plasma *Phys. Rev. Lett.* **109** 185008
- [37] Strickler T S, Langin T K, McQuillen P, Daligault J and Killian T C 2016 Experimental measurement of self-diffusion in a strongly coupled plasma *Phys. Rev. X* **6** 021021
- [38] Vlastós A E 1973 Instabilities of electrically exploded wires *J. Appl. Phys.* **44** 1616
- [39] Walker D N 1986 Perpendicular ion beam-driven instability in a multicomponent plasma: effects of varying ion composition on linear flute mode oscillations *J. Geophys. Res.: Space Phys.* **91** 3305
- [40] Shelkovenko T A, Sinars D B, Pikuz S A and Hammer D A 2001 Radiographic and spectroscopic studies of X-pinch plasma implosion dynamics and x-ray burst emission characteristics *Phys. Plasmas* **8** 1305
- [41] Murillo M S 2001 Using Fermi statistics to create strongly coupled ion plasmas in atom traps *Phys. Rev. Lett.* **87** 115003
- [42] Murillo M S 2006 Ultrafast dynamics of strongly coupled plasmas *Phys. Rev. Lett.* **96** 165001
- [43] Witte B B L, Fletcher L B, Galtier E, Gamboa E, Lee H J, Zastrau U, Redmer R, Glenzer S H and Sperling P 2017 Warm dense matter demonstrating non-Drude conductivity from observations of nonlinear plasmon damping *Phys. Rev. Lett.* **118** 225001
- [44] McKelvey A et al 2017 Thermal conductivity measurements of proton-heated warm dense aluminum *Sci. Rep.* **7** 7015
- [45] Gericke D O, Murillo M S and Schlages M 2002 Dense plasma temperature equilibration in the binary collision approximation *Phys. Rev. E* **65** 036418
- [46] Murillo M S and Dharma-wardana M W C 2008 Temperature relaxation in hot dense hydrogen *Phys. Rev. Lett.* **100** 205005
- [47] Glosli J N, Graziani F R, More R M, Murillo M S, Streit F H, Surh M P, Benedict L X, Hau-Riege S, Langdon A B and London R A 2008 Molecular dynamics simulations of temperature equilibration in dense hydrogen *Phys. Rev. E* **78** 025401(R)
- [48] Cho B I, Ogitsu T, Engelhorn K, Correa A A, Ping Y, Lee J W, Bae L J, Prendergast D, Falcone R W and Heimann P A 2016 Measurement of electron-ion relaxation in warm dense copper *Sci. Rep.* **6** 18843
- [49] Ecker G and Kröll W 1963 Lowering of the ionization energy for a plasma in thermodynamic equilibrium *Phys. Fluids* **6** 62
- [50] Stewart J C and Pyatt K D 1966 Lowering of ionization potentials in plasmas *Astrophys. J.* **144** 1203
- [51] Crowley B J B 2014 Continuum lowering—a new perspective *HEDP* **13** 84
- [52] Ciricosta O et al 2012 Direct measurements of the ionization potential depression in a dense plasma *Phys. Rev. Lett.* **109** 065002
- [53] Vinko S M, Ciricosta O and Wark J S 2014 Density functional theory calculations of continuum lowering in strongly coupled plasmas *Nat. Commun.* **5** 3533
- [54] Fletcher L B et al 2014 Observations of continuum depression in warm dense matter with x-ray Thomson scattering *Phys. Rev. Lett.* **112** 145004
- [55] Ciricosta O, Vinko S M, Barbrel B, Rackstraw D S, Preston T R, Burian T, Chalupský J, Cho B I, Chung H-K and Dakovski G L 2016 Measurements of continuum lowering in solid-density plasmas created from elements and compounds *Nat. Commun.* **7** 11713
- [56] Lindl J 1995 Development of the indirect-drive approach to inertial confinement fusion and the target physics basis for ignition and gain *Phys. Plasmas* **2** 3933
- [57] Betti R, Goncharov V N, McCrory R L and Verdon C P 1998 Growth rates of the ablative Rayleigh–Taylor instability in inertial confinement fusion *Phys. Plasmas* **5** 1446
- [58] Benedict L X et al 2017 Molecular dynamics studies of electron-ion temperature equilibration in hydrogen plasmas within the coupled-mode regime *Phys. Rev. E* **95** 043202
- [59] Landen O L and Winfield R J 1985 Laser scattering from dense cesium plasmas *Phys. Rev. Lett.* **54** 1660
- [60] Bataller A, Kappus B, Camara C and Putterman S 2014 Collision time measurements in a sonoluminescing microplasma with a large plasma parameter *Phys. Rev. Lett.* **113** 0243001
- [61] Bataller A, Plateau G R, Kappus B and Putterman S 2014 Blackbody emission from laser breakdown in high-pressure gases *Phys. Rev. Lett.* **113** 075001

- [62] Bannasch G, Killian T C and Pohl T 2013 Strongly coupled plasmas via Rydberg blockade of cold atoms *Phys. Rev. Lett.* **110** 253003
- [63] Murphy D and Sparkes B M 2016 Disorder-induced heating of ultracold neutral plasmas created from atoms in partially filled optical lattices *Phys. Rev. E* **94** 021201(R)
- [64] Lyon M, Bergeson S D, Diaw A and Murillo M S 2015 Using higher ionization states to increase Coulomb coupling in an ultracold neutral plasma *Phys. Rev. E* **91** 033101
- [65] Lyon M, Bergeson S D and Murillo M S 2015 Strongly-coupled plasmas formed from laser-heated solids *Sci. Rep.* **5** 15693
- [66] Zastrau U 2014 Resolving ultrafast heating of dense cryogenic hydrogen *Phys. Rev. Lett.* **112** 105002
- [67] Gericke D O, Murillo M S, Semkat D, Bonitz M and Kremp D 2003 Relaxation of strongly coupled Coulomb systems after rapid changes of the interaction potential *J. Phys. A: Math. Gen.* **36** 6087
- [68] Zheng J, Chen Q F, Gu Y J, Chen Z Y and Li C J 2014 Thermodynamics, compressibility, and phase diagram: shock compression of supercritical fluid xenon *J. Chem. Phys.* **141** 124201
- [69] Driver K P and Militzer B 2017 First-principles simulations of warm dense lithium fluoride *Phys. Rev. E* **95** 043205
- [70] Pribram-Jones A, Grabowski P E and Burke K 2016 Thermal density functional theory: time-dependent linear response and approximate functionals from the fluctuation-dissipation theorem *Phys. Rev. Lett.* **116** 233001
- [71] Ross M and McMahan A K 1980 Condensed xenon at high pressure *Phys. Rev. B* **21** 1658
- [72] Belonoshko A B, LeBacq O, Ahuja R and Johansson B 2002 Molecular dynamics study of phase transitions in Xe *J. Chem. Phys.* **117** 7234
- [73] Oh J Y, Koo Y H, Cheon J S, Lee B H and Sohn D S 2008 Molecular dynamics simulation of the pressure–volume–temperature data of xenon for a nuclear fuel *J. Nucl. Mater.* **372** 89
- [74] Stanton L G and Murillo M S 2016 Ionic transport in high-energy-density matter *Phys. Rev. E* **93** 043203
- [75] Saha M N LIII 1920 Ionization in the solar chromosphere *Phil. Mag.* **40** 472
- [76] Saha M N 1921 On a physical theory of stellar spectra *Proc. R. Soc. A* **99** 135
- [77] Zaghloul M R, Bourham M A and Doster J M 2000 A simple formulation and solution strategy of the Saha equation for ideal and non-ideal plasmas *J. Phys. D: Appl. Phys.* **33** 977
- [78] Itou H, Amano T and Hoshino M 2014 First-principles simulations of electrostatic interactions between dust grains *Phys. Plasmas* **21** 123707
- [79] Lyon M, Bergeson S D and Murillo M S 2013 Limit of strong ion coupling due to electron shielding *Phys. Rev. E* **87** 033101
- [80] Stanton L G and Murillo M S 2015 Unified description of linear screening in dense plasmas *Phys. Rev. E* **91** 033104
- [81] Hansen J P and McDonald I R 1978 Microscopic simulation of a hydrogen plasma *Phys. Rev. Lett.* **41** 1379
- [82] Lado F 1967 Effective potential description of the quantum ideal gases *J. Chem. Phys.* **47** 5369
- [83] Jones C S and Murillo M S 2007 Analysis of semi-classical potentials for molecular dynamics and Monte Carlo simulations of warm dense matter *HEDP* **3** 379
- [84] Diaw A and Murillo M S 2017 A viscous quantum hydrodynamics model based on dynamic density functional theory *Sci. Rep.* **7** 15352
- [85] Cowley C (<http://www-personal.umich.edu/~cowley/ionen.htm>)
- [86] Rouse C A 1961 Ionization equilibrium equation of state *Astrophys. J.* **134** 435
- [87] Ott T, Bonitz M, Stanton L G and Murillo M S 2014 Coupling strength in Coulomb and Yukawa one-component plasmas *Phys. Plasmas* **21** 113704
- [88] Dharma-wardana M W C and Murillo M S 2008 Pair-distribution functions of two-temperature two-mass systems: comparison of molecular dynamics, classical-map hypernetted chain, quantum Monte Carlo, and Kohn–Sham calculations for dense hydrogen *Phys. Rev. E* **77** 026401
- [89] Archer A J, Pini D, Evans R and Reatto L 2007 Model colloidal fluid with competing interactions: bulk and interfacial properties *J. Chem. Phys.* **126** 014104
- [90] Eliezer S, Ghatak A K and Hora H 2002 *Fundamentals of Equations of State* (Singapore: World Scientific)
- [91] Hu S X, Militzer B, Goncharov V N and Skupsky S 2010 Strong coupling and degeneracy effects in inertial confinement fusion implosions *Phys. Rev. Lett.* **104** 235003
- [92] Caillabet L, Canaud B, Salin G, Mazevet S and Loubeyre P 2011 Change in inertial confinement fusion implosions upon using an *ab initio* multiphase DT equation of state *Phys. Rev. Lett.* **107** 115004
- [93] Salpeter E E 1960 Electron density fluctuations in a plasma *Phys. Rev.* **120** 1528
- [94] Boercker D B and More R M 1986 Statistical mechanics of a two-temperature, classical plasma *Phys. Rev. A* **33** 1859
- [95] Seufferling P, Vogel J and Toepffer C 1989 Correlations in a two-temperature plasma *Phys. Rev. A* **40** 323
- [96] Potekhin A Y, Chabrier G and Rogers F J 2009 equation of state of classical Coulomb plasma mixtures *Phys. Rev. E* **79** 016411
- [97] Fletcher A, Close S and Mathias D 2015 Simulating plasma production from hypervelocity impacts *Phys. Plasmas* **22** 093504
- [98] Abe R 1959 Giant cluster expansion theory and its application to high temperature plasma *Prog. Theor. Phys.* **22** 213
- [99] Brush S G, Sahlin H L and Teller E 1966 Monte Carlo study of a one component plasma. I *J. Chem. Phys.* **45** 2102
- [100] Dahan M B, Peik E, Reichel J, Castin Y and Salomon C 1996 Bloch oscillations of atoms in an optical potential *Phys. Rev. Lett.* **76** 4508
- [101] Huber R, Tauser F, Brodschelm A, Bichler M, Abstreiter G and Leitenstorfer A 2001 How many-particle interactions develop after ultrafast excitation of an electron–hole plasma *Nature* **414** 286
- [102] Zhang W, Azad A K and Grischkowsky D 2003 Terahertz studies of carrier dynamics and dielectric response of n-type, freestanding epitaxial GaN *Appl. Phys. Lett.* **82** 2841
- [103] Agrawal A, Matsui T, Zhu W, Nahata A and Vardeny Z V 2009 Terahertz spectroscopy of plasmonic fractals *Phys. Rev. Lett.* **102** 113901
- [104] Nouvel P, Marinchio H, Torres J, Palermo C, Gasquet D, Chusseau L, Varani L, Shiktorov P, Starikov E and Gruzinskis V 2009 Terahertz spectroscopy of plasma waves in high electron mobility transistors *J. Appl. Phys.* **106** 013717